PCCP

PAPER

View Article Online
View Journal | View Issue

Cite this: *Phys. Chem. Chem. Phys.*, 2019, **21**, 22611

Low-dimensional functional networks of cage-like B_{40} with effective transition-metal intercalations†

Wen-Yan Zan, * Hai-Ru Li, Yue-Wen Mu, * Hai-Gang Lu and Si-Dian Li *

Received 9th June 2019,
Accepted 17th September 2019

DOI: 10.1039/c9cp03252e

rsc.li/pccp

As the first all-boron fullerene observed in experiments, cage-like borospherene B_{40} has attracted considerable attention in recent years. However, B_{40} has been proved to be chemically reactive and tends to coalesce with one another *via* the formation of covalent bonds. We explore herein the possibility of low-dimensional functional networks of B_{40} with effective transition-metal intercalations. We find that the four equivalent B_7 heptagons on the waist of each B_{40} can serve as effective ligands to coordinate various transition metal centers in exohedral motifs. The intercalated metal atoms entail these networks with a variety of intriguing properties. The two-dimensional (2D) Cr_2B_{40} network is a ferromagnetic metal while the 2D Zn_2B_{40} network becomes semiconducting. In contrast, other 2D M_2B_{40} (M = Sc, Ti, V, Mn, Fe, Co, Ni and Cu) networks and 1D CrB_{40} belong to nonmagnetic metals. The 3D Cr_3B_{40} network is a magnetic metal. This work presents the viable possibility of assembling M_n&B_{40} metalloborospherenes into stable functional nanomaterials *via* effective transition-metal intercalations with potential applications in electronic and spintronic devices.

1. Introduction

Fullerenes are a set of cage-like carbon molecules that have particular properties and important applications in various areas.[1] The discovery of fullerenes stimulates great interest in other zero-dimensional cage-like nanoclusters, especially homoelemental cage structures. Over the past three decades, great effort has been devoted to finding the next element capable of constructing hollow cages. As a light neighbour of carbon in the periodic table, boron is among the most promising choices. However, different from carbon, boron tends to form multicenter two-electron bonds in both bulk allotropes and polyhedral molecules to compensate for its electron deficiency. The first perfect cage-like I_h B_{80}^{2} as an electron equivalent of I_h C_{60} was proposed in 2007. Although further theoretical work showed that B_{80} favours core–shell structures in thermodynamics,[3,4] the unique configuration of B_{80} has attracted considerable attention for all-boron fullerenes. In a joint experimental and theoretical investigation reported in 2014, Zhai and co-workers discovered the first all-boron fullerenes D_{2d} $B_{40}^{-/0}$, called borospherenes, which are composed of twelve interwoven boron double chains with two B_6 hexagons on the top and bottom and four B_7 hexagons on the waist, with twelve delocalized π bonds around the hexagonal and heptagonal rings over the cage surface.[5] Although the D_{2d} B_{40}^{-} monoanion appears to be slightly less stable than the quasi-planar C_s B_{40}^{-} global minimum with two adjacent hexagonal rings, cage-like D_{2d} B_{40} is the well-defined global minimum of the neutral. The first axially chiral borospherenes C_3/C_2 B_{39}^{-} were observed in experiments shortly after and a series of borospherenes (B_{38}, B_{39}^{+}, B_{40}^{+}, B_{28}, B_{29}^{-}, B_{44}, B_{44}^{-}, B_{41}^{+}, B_{42}^{2+}, B_{46}, B_{37}^{-}, and B_{38}^{-}) were theoretically predicted later.[6–16]

The diameter (6.2 Å) of B_{40} is slightly smaller than that (7.1 Å) of C_{60}, which enables B_{40} to accommodate a series of metal atoms or small molecules comfortably inside. Meanwhile, the heptagonal and hexagonal rings on the cage surface of B_{40} make it possible to coordinate metal atoms in an exohedral manner. Theoretical calculations have indicated that B_{40} fullerenes can be decorated with different types of metal atoms, including alkaline earth metals, alkaline metals, transition metals, lanthanide metals, and actinide metals.[17–24] Bai *et al.* reported the first perfect endohedral M@B_{40} (M = Ca and Sr) with a metal atom at the center and exohedral M&B_{40} (M = Be and Mg) with a metal center face-capping a heptagon on the waist to form metalloborospherenes, at the density functional theory (DFT) level.[17] Fa *et al.* found that the Na and Ba atoms prefer staying inside the B_{40} cage, while the Li, K, and Ti atoms favour exohedral configurations.[18] Li *et al.* predicted the existence of stable exohedral metalloborospherenes Ni_n&B_{40} (n = 1–4) with effective Ni–B_{40} coordination and their two-dimensional precursor $Ni_2 \in B_{14}$, presenting the possibility of metalloborospherenes with heptacoordinate Ni centers.[23] Theoretical studies of Jin *et al.* showed that it is possible to experimentally achieve endohedral M@B_{40} (M = Sc, Y, and La).[19] In another recent theoretical study, a unique actinide-encapsulated

Institute of Molecular Science, Shanxi University, Taiyuan, 034000, China. E-mail: zanwy@sxu.edu.cn, lisidian@sxu.edu.cn

† Electronic supplementary information (ESI) available. See DOI: 10.1039/c9cp03252e

U@B_{40} cage structure was predicted.[20] The high stabilities of exohedral metalloborospherenes inspire us to consider whether such metalloborospherenes can be used as essential building blocks to form 1D, 2D and 3D crystalline materials to realize the assembly of B_{40} which has been proved to have a reactive surface.[25] Some theoretical investigations have predicted that the boron-cluster unit can be used to design stable low-dimensional boron systems.[26–28] Wang *et al.* predicted cluster-assembled materials of B_{40} which are thermodynamically stable with semiconducting features.[29] However, to the best of our knowledge, there have been no theoretical or experimental investigations reported to date on metalloborospherene-assembled nanomaterials. We anticipate that transition-metal intercalations can help stabilize boron networks and modulate the structural and electronic properties of the B_{40}-assembled materials. Transition-metal intercalation has been theoretically proved to be an effective way to modulate the electronic and magnetic properties of bilayer borophenes.[30,31] Theoretical studies of Zhang *et al.* showed that the structure of 2D boron sensitively depends on the metal substrate.[32–35]

Here, we present a systematic computational investigation of the $B_{40}CrB_{40}$ sandwich cluster; 1D, 2D and 3D Cr_nB_{40} networks (n = 1–3); and 2D M_2B_{40} (M = Sc, Ti, V, Mn, Fe, Co, Ni, Cu and Zn) at the density functional theory level, aiming to design novel nanomaterials assembled from exohedral metalloborospherenes with novel properties and potential applications. Our results show that 1D CrB_{40} and 2D Cr_2B_{40} networks are thermodynamically stable which maintain the structural integrity of the B_{40} cages during molecular dynamic simulations. We found that the 2D Cr_2B_{40} network is a ferromagnetic conductor, 2D M_2B_{40} (M = Sc, Ti, V, Mn, Fe, Co, Ni and Cu) networks are nonmagnetic metals, and 2D Zn_2B_{40} is an indirect-gap semiconductor. This work presents a possible route to synthesize cluster-assembled boron nanomaterials using exohedral metalloborospherenes as building blocks.

2. Computational methods

Density functional theory calculations were carried out by using the Vienna Ab initio Simulation Package (VASP) code.[36,37] The projector augmented wave (PAW) method[38,39] for potentials at the core region and spin-polarized DFT based on the generalized gradient approximation (GGA) of PBE functional were adopted.[40] A kinetic energy cut-off of 400 eV was used for the plane-wave expansion. The k-point grids in the first Brillouin zone of 1D, 2D and 3D MB_{40} networks were 1 × 8 × 1, 8 × 8 × 1 and 8 × 8 × 4, respectively. All atomic positions were fully relaxed using the conjugate gradient method until the force on each atom was less than 0.01 eV $Å^{-1}$. Vacuum layers of 15 Å between two B_{40} monoplanes or between two B_{40} chains were used to prevent mirror interactions. The $B_{40}CrB_{40}$ cluster was fully optimized with frequencies checked at PBE0 levels[41] with the 6-31G* basis set using the Gaussian 09 program.[42] Zero-point corrections were considered in cluster energy calculations. Molecular dynamics (MD) simulations were performed for 1D and 2D Cr_nB_{40} networks for 10 ps at room temperature with the mixed Gaussian and Plane-Waves (GPW) method, as implemented within the CP2K code. Goedecker–Teter–Hutter pseudopotentials and the DZVP MOLOPT basis set were adopted.[43] The binding energy (E_b) per coordination site of the M_nB_{40} networks was calculated using the expression:

$$E_b = (E_{B_{40}} + nE_{TM} - E_{total})/n \quad (1)$$

where E_{total} represents the total energy of M_nB_{40} networks and n is the number of transition-metal atoms in a M_nB_{40} unit cell. $E_{B_{40}}$ and E_{TM} are the energies of a single B_{40} cage and a single transition-metal atom in vacuum, respectively.

The coordination energy (E_c) per coordination site of the M_nB_{40} networks or the $B_{40}CrB_{40}$ cluster between the transition-metal center and its B_{40} ligands was calculated using the expression:

$$E_c = (E_{B_{40}'} + nE_{TM} - E_{total})/n \quad (2)$$

where E_{total} represents the total energy of the M_nB_{40} networks or a $B_{40}CrB_{40}$ cluster and n is the number of transition atoms in a M_nB_{40} unit cell or a $B_{40}CrB_{40}$ cluster. $E_{B_{40}'}$ and E_{TM} are the corresponding energies of the B_{40} frameworks or a $(B_{40})_2$ dimer and the single transition-metal atom in vacuum, respectively.

The charge density difference of the M_nB_{40} networks was calculated using the expression:

$$\Delta\rho = \rho_{total} - \rho_{B_{40}} - \rho_{TM} \quad (3)$$

where ρ_{total} represents the charge density of M_nB_{40} networks and $\rho_{B_{40}}$ and ρ_{TM} are the charge densities of the isolated B_{40} cages and the isolated transition-metal atoms at the same positions in M_nB_{40} networks, respectively.

Chemical bonding analyses of the one-dimensional CrB_{40} network were performed using the solid-state adaptive natural density partitioning (SSAdNDP) method,[44] which is an extension of the AdNDP method.[45] Both methods (AdNDP and SSAdNDP) were derived from the natural bonding orbital (NBO) method developed for molecules and periodic systems.[46,47] The same parameters were used for periodic NBO and SSAdNDP analyses as in VASP calculations. The Visualization for Electronic and Structural Analysis software (VESTA, series 3)[48] was used for visualization of the SSAdNDP results.

3. Results and discussion

3.1 Geometries and stabilities of the $B_{40}CrB_{40}$ cluster

The B_{40} cage consists of two B_6 hexagonal rings at the top and bottom, four B_7 heptagonal rings evenly distributed on the waist, and forty-eight B_3 triangles on twelve interwoven boron double chains (Fig. 1). Its twelve radial π orbitals around the six B_7 heptagonal or B_6 hexagonal rings are similar to the π orbitals of benzene. By mimicking dibenzenechromium D_{6h} $C_6H_6CrC_6H_6$,[49] a prototypical transition-metal complex with a Cr center sandwiched between two C_6H_6 ligands, we built a set of $B_{40}CrB_{40}$ structures with C_{2h} or C_{2v} symmetry, in which the heptagons or hexagons of each B_{40} cage served as ligands to coordinate with the Cr centers. After full structural optimizations, the most stable geometry of the $B_{40}CrB_{40}$ cluster was observed shown in Fig. 1. The $B_{40}CrB_{40}$

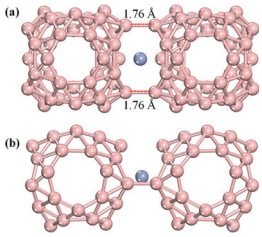

Fig. 1 Optimized geometric structure of the C_{2v} $B_{40}CrB_{40}$ cluster (a) top view with B–B bond lengths between the two B_{40} ligands indicated and (b) the side view. Pink and blue spheres stand for the B and Cr atoms, respectively.

cluster was found to be a true minimum with no imaginary frequencies. It has C_{2v} symmetry, where the heptagon of one cluster stacks parallel onto that of the other in an eclipsed motif, with the Cr atom located in the middle between the two B_{40} ligands. All possible spin multiplicities have been considered during relaxation of the $B_{40}CrB_{40}$ clusters. The most stable one is found to have a spin of $S = 5$. It is noticed that the two B_{40} cages do not exhibit significant distortions in the optimized $B_{40}CrB_{40}$. The B–B distances of r_{B-B} = 1.76 Å between the two B_{40} cages indicate that σ-covalent interactions are formed between the neighboring B_{40} ligands, while the Cr–B distances of r_{Cr-B} = 2.19–2.39 Å indicate the formation of effective coordination interactions between Cr and B_{40} ligands. The calculated coordination energy of C_{2v} $B_{40}CrB_{40}$ in eqn (2) was E_c = 8.29 eV, indicating that effective coordination interactions were formed between the Cr center and the two B_{40} ligands. Wang *et al.* predicted that a $7_3 \perp 7_1$ $(B_{40})_2$ dimer possesses lower energy than other isomers, namely, the 7_3 heptagon of one B_{40} stacks onto the vertical 7_1 heptagon of the other (the four heptagons around the waist in the B_{40} cage are denoted as 7_1, 7_2, 7_3 and 7_4).[29] Based on this configuration, we constructed and optimized the Cr intercalated $7_3 \perp 7_1$ $B_{40}CrB_{40}$ double-deck complex and compared the stabilities of the $7_3 \perp 7_1$ B_{40} dimer intercalated by the Cr atom (see Fig. S1, ESI†) and the C_{2v} $B_{40}CrB_{40}$ cluster. Our results show that the eclipsed C_{2v} $B_{40}CrB_{40}$ cluster is more stable than the $7_3 \perp 7_1$ $B_{40}CrB_{40}$ dimer by about 0.31 eV lower in energy, showing that our eclipsed $B_{40}CrB_{40}$ is favored in thermodynamics. We further studied the Cr-encapsulated $B_{40}CrB_{40}$ cluster (see Fig. S2, ESI†) and found that this cluster is energetically less stable by 2.87 eV than the eclipsed C_{2v} $B_{40}CrB_{40}$ cluster.

The calculated natural atomic charge of the Cr center is q_{Cr} = +1.27 $|e|$ in $B_{40}CrB_{40}$, well in line with the electronic configurations of Cr $[Ar]4s^{0.28}3d^{4.44}$. Each Cr center thus donates approximately two 4s electrons to the boron framework and, in return, accepts about one electron *via* back-donations from the B_{40} cage to the partially filled 3d orbitals of Cr. The Cr center possesses a total Wiberg bond order of WBI_{Cr} = 3.65, with an average Cr–B coordination bond order of WBI_{Cr-B} = 0.19. These results indicate again that effective covalent coordination interactions are formed in $B_{40}CrB_{40}$.

3.2 Geometries and stabilities of 1D, 2D and 3D Cr_nB_{40} (n = 1–3) networks and M_2B_{40} networks

We constructed 1D CrB_{40}, 2D Cr_2B_{40} and 3D Cr_3B_{40} networks based on the optimized C_{2v} $B_{40}CrB_{40}$ (see Fig. 1). The fully

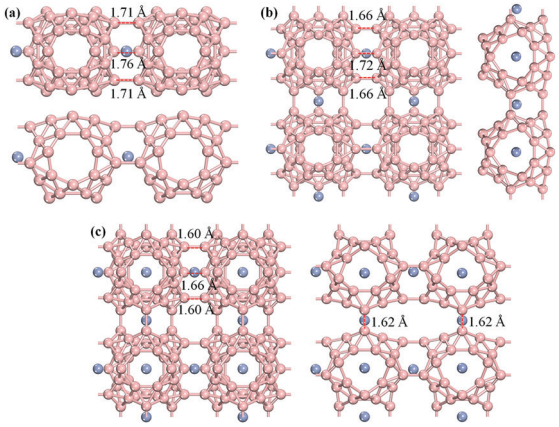

Fig. 2 Most stable configurations of (a) the 1D CrB_{40} network. Up: the top view and down: the front view; (b) the 2D Cr_2B_{40} network. Left is the top view and right is the front view; (c) the 3D Cr_3B_{40} network. Left is the top view and right is the front view.

relaxed configurations of 1D $Pmm2$ CrB_{40}, 2D $P\bar{4}m2$ Cr_2B_{40}, and 3D $P4_2/mmc$ Cr_3B_{40} networks are shown in Fig. 2. The one-dimensional Cr B_{40} network in the x direction is composed of alternate Cr atoms and B_{40} units in eclipsed motifs, with a structural feature similar to that of the PdC_{60} network.[50] We also checked the energy of other 1D Cr B_{40} networks with different conformations (see Fig. S3, ESI†), and the eclipsed conformation discussed above appears to have the lowest energy. 2D $P\bar{4}m2$ Cr_2B_{40} (in $x$and y directions) and 3D $P4_2/mmc$ Cr_3B_{40} (in x, y, and z directions) networks are designed based on the extensions of the $Pmm2$ 1D CrB_{40} network in 2D and 3D directions, respectively. In particular, along the z axis of 3D $P4_2/mmc$ Cr_3B_{40} networks, the hexagons of one B_{40} prefer to stack parallel onto those of the other. The B_{40} molecules are covalently bonded with one another in these networks, with Cr centers exohedrally coordinated between two neighboring B_{40} cages. The distances between the neighboring B_{40} cages lie in the range between 1.60 and 1.76 Å, similar to that of the intericosahedral links in β-rhombohedral boron (1.65–1.75 Å).[51] It is noticed that the Cr atoms favor exohedral locations in the middle between the two adjacent B_{40} cages. The lattice parameters of 1D, 2D, and 3D Cr_nB_{40} networks are 7.63 Å, 7.66 Å/7.66 Å, and 7.46 Å/7.46 Å/14.74 Å, in the a, a/b and $a/b/c$ directions, respectively. Their dynamic stabilities are confirmed by performing extensive molecular dynamics (MD) simulations. We carried out MD simulations on 1D $Pmm2$ and 2D $P\bar{4}m2$ Cr_nB_{40} networks at room temperature (T = 300 K) with a time step of 1 fs. After 10 000 steps, their geometries were well maintained, suggesting that 1D $Pmm2$ and 2D $P\bar{4}m2$ Cr_nB_{40} networks are thermodynamically stable. To describe the binding strength between Cr atoms and B_{40} cages in 1D CrB_{40}, 2D Cr_2B_{40} and 3D Cr_3B_{40} networks, we calculate their binding energies per coordination site using eqn (1) which turn out to be E_b = 8.62 eV, 9.39 eV and 8.55 eV, respectively. Interestingly, the 2D Cr_2B_{40} network possesses the highest binding energies in the series. Extension in the z direction perpendicular to the B_6 hexagonal rings of the B_{40} units appears to be less favourable

in binding energy relative to extensions in 1D (x) or 2D (x and y) directions perpendicular to B_7 heptagons. The calculated coordination energies per coordination site of 1D CrB_{40}, 2D Cr_2B_{40}, and 3D Cr_3B_{40} networks using eqn (2) are E_c = 7.62 eV, 7.25 eV and 7.15 eV, respectively, indicating that, relative to the corresponding binding energies (E_b) discussed above, transition-metal-B_{40} coordination intercalations play the major role (77–85%) in stabilizing the Cr_nB_{40} networks, with B–B σ-interactions between the adjacent B_{40} cages contributing less than 25% in the Cr_nB_{40} series (n = 1–3). 1D $Pmm2$, 2D $P\bar{4}m2$ and 3D $P4_2/mmc$ Cr_nB_{40} networks all appear to be metallic in nature.

Other 3d transition metal atoms (Sc, Ti, V, Mn, Fe, Co, Ni, Cu and Zn) turn out to form similar intercalated 2D M_2B_{40} networks. Table 1 shows the binding energies (E_b) and the corresponding coordination energies (E_c) per coordination site between B_{40} and 3d transition metals, the total magnetic moments (MM) per unit cell and the charge loss (e) of 3d transition metals from Bader charge analyses of the M_2B_{40} networks. The calculated binding energies of 2D M_2B_{40} networks were in the order of V_2B_{40} > Ti_2B_{40} > Sc_2B_{40} > Fe_2B_{40} > Co_2B_{40} > Cr_2B_{40} > Mn_2B_{40} > Ni_2B_{40} > Cu_2B_{40} > Zn_2B_{40} and the calculated coordination energies of 2D M_2B_{40} networks exhibited the same variation trend, with Cu_2B_{40} and Zn_2B_{40} having completely filled $3d^{10}$ orbitals and possessing the lowest E_b and E_c values (see Table 1 and Fig. 3). V and Ti atoms among the 3d transition metals are the best choices to use to assemble B_{40} cages with the highest binding energies and coordination energies. The high stabilities of M_2B_{40} (M = Sc, Ti, V, Cr, Mn, Fe, Co and Ni) networks are related to the p–d back-donations, where a certain amount of electrons in B_{40} was reversely transferred to the empty d levels of 3d transition metals.[17]

To explore the binding properties, the charge density differences of M_2B_{40} networks were calculated. The charge distributions of the M_2B_{40} networks appear to be similar to those of 2D Cr_2B_{40} as shown in Fig. 4a. It is shown that the electrons of Cr atoms were transferred to B_{40} cages and noticeable charge accumulations between the B_{40} ligands and Cr centers were observed, indicating the covalent coordination bonding nature of Cr–B_{40} interactions. Similar to the situation in Cr@BHBs,[31] charges are depleted from the Cr atom and accumulated around the Cr–B coordination bonds. Such bonding character can also be recognized from the partial density of states

Table 1 Calculated binding energies per coordination site (E_b), coordination energies per coordination site (E_c), total magnetic moments (MM) per unit cell, and charge loss (q) of 3d transition metals from Bader charge analyses of 2D M_2B_{40} networks

2D M_2B_{40}	E_b (eV)	E_c (eV)	MM (μ_B)	q (e)
Sc_2B_{40}	10.28	8.14	0	2.66
Ti_2B_{40}	12.21	10.07	0	2.65
V_2B_{40}	12.34	10.20	0	2.32
Cr_2B_{40}	9.39	7.25	2.03	1.86
Mn_2B_{40}	9.03	6.89	0	1.32
Fe_2B_{40}	9.80	7.66	0	0.95
Co_2B_{40}	9.79	7.65	0	0.70
Ni_2B_{40}	8.85	6.71	0	0.71
Cu_2B_{40}	6.33	4.19	0	1.00
Zn_2B_{40}	3.51	1.37	0	1.81

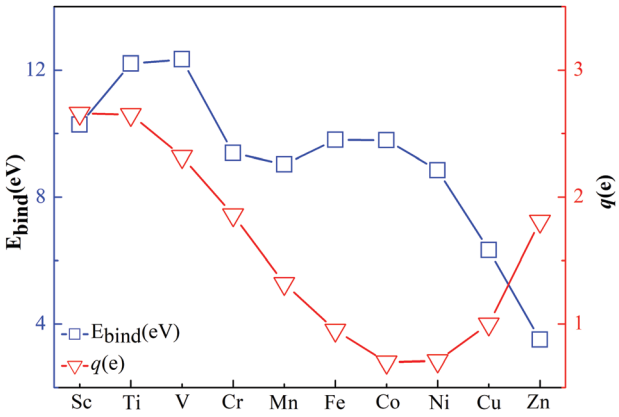

Fig. 3 Binding energies per coordination site of 2D M_2B_{40} networks (blue) and the electrons transferred from 3d transition metals to B_{40} networks (red).

(PDOS) plots (see Fig. 8b), wherein a remarkable hybridization of B-p and Cr-d near the Fermi level is formed. Quantitatively, based on Bader charge analysis, there was a 0.70–2.66 $|e|$ charge transfer from 3d transition metals to B_{40} cages (see Table 1). The electron transfers in Cu_2B_{40} and Zn_2B_{40} are 1 $|e|$ and 1.81 $|e|$, respectively, to form completely filled 3d orbitals ($3d^{10}$) in Cu and Zn. Except for Cu and Zn, the charges transferred to the B_{40} cages generally decrease from Sc to Ni (see Fig. 3), and these metals exhibit similar behavior in bilayer borophene intercalated by 3d transition metal atoms.[30] Such a significant electron transfer supports the electron supplement effects in stabilizing the electron-deficient B_{40} networks.

To clarify the chemical bonding of Cr_nB_{40} networks, we took 1D CrB_{40} as an example to perform a solid-state adaptive natural density (SSAdNDP) analysis.[44] The results of SSAdNDP analyses show that 1D CrB_{40} possesses a σ + π double delocalization bonding pattern on its B_{40} frameworks, which is well in line with the bonding patterns of a cage-like B_{40} unit.[5] The unique σ and π bonding interactions around the coordination site in 1D CrB_{40} are displayed in Fig. 5. SSAdNDP analysis recovered 3 2c-2e B–B σ-bonds with occupation numbers of ON = 1.73 $|e|$ between the adjacent B_{40} cages in 1D CrB_{40}, showing the covalent bonding interaction between two neighboring B_{40} cages. More interestingly, it revealed 2 6c-2e π bonds with ON = 1.99 $|e|$, 2 8c-2e π bonds with ON = 1.73 $|e|$, and 4 7c-2e π bonds with ON = 1.66–1.98 $|e|$ between the Cr center and its two B_{40} ligands, showing the formation of effective Cr–B_{40} coordination interactions *via* partial d–p π overlap.

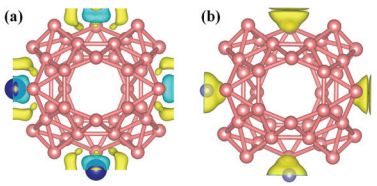

Fig. 4 (a) Charge density difference and (b) spin density distribution for the 2D Cr_2B_{40} network. The isosurface levels for charge density difference are 0.01 e $Bohr^{-3}$ (yellow) and −0.01 e $Bohr^{-3}$ (blue) and the isosurface levels for spin density are 0.008 e $Bohr^{-3}$ (yellow) and −0.008 e $Bohr^{-3}$ (blue).

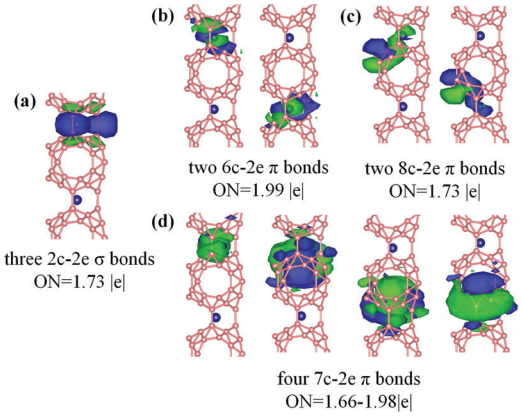

Fig. 5 SSAdNDP chemical bonding pattern of the 1D CrB_{40} network.

3.3 Electronic and Magnetic properties of M_nB_{40} networks

More interestingly and encouragingly, these 2D M_2B_{40} (M = Sc, Ti, V, Cr, Mn, Fe, Co, Ni, Cu and Zn) networks exhibit intrinsically different electronic properties. 2D M_2B_{40} (Sc, Ti, V, Cr, Mn, Fe, Co, Ni and Cu) networks are metals, while the 2D Zn_2B_{40} network is a semiconductor with an indirect band gap of 0.40 eV (see Fig. 6). For the 2D Zn_2B_{40} network, the density of states near the Fermi level is mainly contributed by the 2p orbital of B atoms (see Fig. S4, ESI†), while the density of states near the Fermi level in the Cr_2B_{40} network is composed of the 2p orbital of B atoms and the 3d orbital of Cr atoms (see Fig. 8b). Meanwhile, during the relaxation of these structures, both spin-unpolarized and spin-polarized computations were carried out to determine the ground state for a series of M_nB_{40} networks. It is found that the 1D CrB_{40} network is a nonmagnetic metal, while the 3D Cr_3B_{40} network is a magnetic metal (see Fig. 6). It is shown that the 2D Cr_2B_{40} network has a ferromagnetic state, as the spin-polarized total energy is lower than the spin-unpolarized one. However, for the 2DM_nB_{40} network, the systems decorated with other 3d transition metals have nonmagnetic ground states. We have found that the 2D Cr_2B_{40}

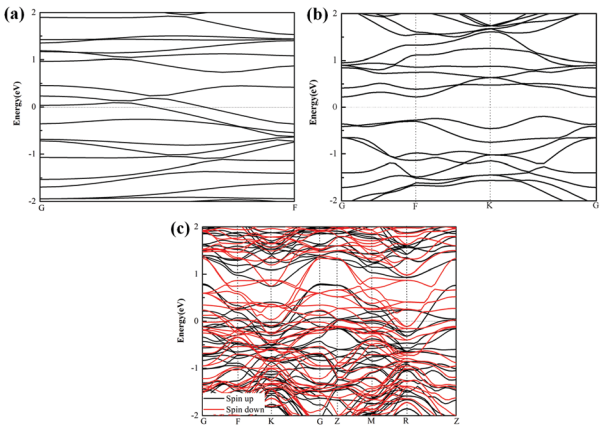

Fig. 6 Calculated band structures for the (a)1D CrB_{40} network. (b) 2D Zn_2B_{40} network. (c) 3D Cr_3B_{40} network. *G* = (0, 0, 0), *F* = (0, 0.5, 0), *K* = (0.5, 0.5, 0), *Z* = (0, 0, 0.5), *M* = (0, 0.5, 0.5), and *R* = (0.5, 0.5, 0.5). *G* presents the *Γ* point.

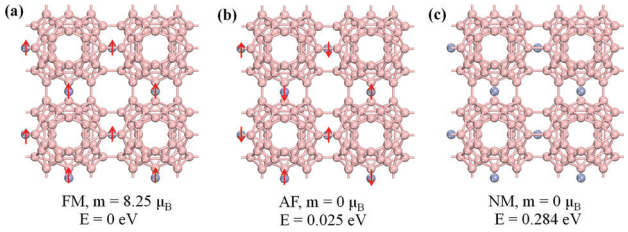

Fig. 7 Different magnetic configurations of the 2D Cr_2B_{40} network with their magnetic moments and relative energies indicated for (a) ferromagnetic, (b) antiferromagnetic, and (c) nonmagnetic configurations.

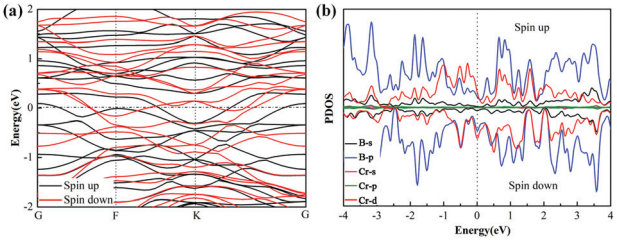

Fig. 8 (a) Calculated band structure of the 2D Cr_2B_{40} network. (b) Projected density of states (PDOS) for 2D Cr_2B_{40}.

network has a ferromagnetic ground state and a total magnetic moment of 2.03 μ_B per unit cell. Here two Cr atoms per unit cell carry magnetic moments of 2.03 μ_B, whereas the magnetic moment of B atoms in the B_{40} cage is nearly zero. To gain further insight and clarity on the origin of the magnetism, spin density distribution on the 2D Cr_2B_{40} network is plotted in Fig. 4b. As shown in Fig. 4b, the induced magnetic moments are mainly localized on Cr atoms, while the contribution of B atoms was negligible. In order to investigate the preferred coupling of these moments, ferromagnetic (FM) coupling, antiferromagnetic (AF) coupling, and nonmagnetic (NM) states were considered. Different magnetic configurations of the 2D Cr_2B_{40} network with their magnetic moments and relative energies are shown in Fig. 7. Note that the favourable magnetic configuration of AF coupling is displayed in Fig. 7b. We found that the ground state is FM (Fig. 7a), which lies 0.025 and 0.284 eV lower in energy than the AF and NM states, respectively. According to the energy difference between FM and AF states and the mean field theory,[52] the Curie temperature of the 2D Cr_2B_{40} network was estimated to be 73 K.

To explicitly explain the origin of magnetism in the Cr_2B_{40} network, the spin-polarized band structure and projected density of states of the 2D Cr_2B_{40} network are presented in Fig. 8. As shown in Fig. 8a, both spin channels exhibit metallic features. Examination of the states near the Fermi level shows that the magnetism of the 2D Cr_2B_{40} network is mainly contributed by the d-electrons of Cr atoms (Fig. 8b).

4. Conclusions

We have constructed a number of stable boron networks in different dimensionalities made of B_{40} molecules and transition

metals using comprehensive first-principles calculations. We have scanned a series of transition metals (Sc, Ti, V, Cr, Mn, Fe, Co, Ni, Cu and Zn) and obtained a rich variety of electronic and magnetic properties in M_nB_{40}/networks that can be coded by transition metals. In particular, the 2D Cr_2B_{40} network has a ferromagnetic ground state with a Curie temperature estimated to be 73 K. The polarized electron spins are mainly concentrated on Cr atoms in the 2D network. In contrast, 1D CrB_{40}, 3D Cr_3B_{40}, and the other 2D M_2B_{40} (M = Sc, Ti, V, Mn, Fe, Co, Ni and Cu) networks exhibited metallic properties. An exception is seen for the Zn_2B_{40} network, which is a semiconductor with an indirect band gap of 0.4 eV. We reveal that the charge transfer and coordination interactions between transition metals and B_{40} cages play a critical role in determining the electronic properties of the metalloborospherene networks. Our results not only enrich the understanding of complicated boron–metal interactions but also suggest the potential of turning the B_{40} cluster into functional nanomaterials by transition-metal intercalations in metalloborospherene-assembled nanomaterials.

Conflicts of interest

There are no conflicts to declare.

Acknowledgements

The work was supported by the National Natural Science Foundation of China (21720102006 to S.-D. Li, 21803037 to W.-Y. Zan, 11504213 to Y.-W. Mu, and 21473106 to H.-G. Lu, U1510103) and the Natural Science Foundation of Shanxi Province, China (201801D221060 to W.-Y. Zan)

Notes and references

1 H. W. Kroto, J. R. Heath, S. C. O'Brien, R. F. Curl and R. E. Smalley, *Nature*, 1985, **318**, 162–163.
2 N. G. Szwacki, A. Sadrzadeh and B. I. Yakobson, *Phys. Rev. Lett.*, 2007, **98**, 166804.
3 J. Zhao, L. Wang, F. Li and Z. Chen, *J. Phys. Chem. A*, 2010, **114**, 9969–9972.
4 F. Li, P. Jin, D. Jiang, L. Wang, S. B. Zhang, J. Zhao and Z. Chen, *J. Chem. Phys.*, 2012, **136**, 074302.
5 H. J. Zhai, Y. F. Zhao, W. L. Li, Q. Chen, H. Bai, H. S. Hu, Z. A. Piazza, W. J. Tian, H. G. Lu, Y. B. Wu, Y. W. Mu, G. F. Wei, Z. P. Liu, J. Li, S. D. Li and L. S. Wang, *Nat. Chem.*, 2014, **6**, 727–731.
6 J. Lv, Y. Wang, L. Zhu and Y. Ma, *Nanoscale*, 2014, **6**, 11692–11696.
7 Q. Chen, W. L. Li, Y. F. Zhao, S. Y. Zhang, H. S. Hu, H. Bai, H. R. Li, W. J. Tian, H. G. Lu, H. J. Zhai, S. D. Li, J. Li and L. S. Wang, *ACS Nano*, 2015, **9**, 754–760.
8 X. Y. Zhao, Q. Chen, H. R. Li, Y. W. Mu, H. G. Lu and S. D. Li, *Phys. Chem. Chem. Phys.*, 2017, **19**, 10998–11003.
9 H. R. Li, Q. Chen, X. X. Tian, H. G. Lu, H. J. Zhai and S. D. Li, *J. Mol. Model.*, 2016, **22**, 124.
10 J. Zhao, X. Huang, R. Shi, H. Liu, Y. Su and R. B. King, *Nanoscale*, 2015, **7**, 15086–15090.
11 H. R. Li, T. Jian, W. L. Li, C. Q. Miao, Y. J. Wang, Q. Chen, X. M. Luo, K. Wang, H. J. Zhai, S. D. Li and L. S. Wang, *Phys. Chem. Chem. Phys.*, 2016, **18**, 29147–29155.
12 T. B. Tai and M. T. Nguyen, *Chem. Commun.*, 2016, **52**, 1653–1656.
13 S. Li, Z. Zhang, Z. Long and S. Qin, *Sci. Rep.*, 2017, **7**, 40081.
14 Q. Chen, S. Y. Zhang, H. Bai, W. J. Tian, T. Gao, H. R. Li, C. Q. Miao, Y. W. Mu, H. G. Lu, H. J. Zhai and S. D. Li, *Angew. Chem., Int. Ed.*, 2015, **54**, 8160–8164.
15 T. B. Tai and M. T. Nguyen, *RSC Adv.*, 2017, **7**, 22243–22247.
16 Q. Chen, W. J. Tian, L. Y. Feng, H. G. Lu, Y. W. Mu, H. J. Zhai, S. D. Li and L. S. Wang, *Nanoscale*, 2017, **9**, 4550–4557.
17 H. Bai, Q. Chen, H. J. Zhai and S. D. Li, *Angew. Chem., Int. Ed.*, 2015, **54**, 941–945.
18 W. Fa, S. Chen, S. Pande and X. C. Zeng, *J. Phys. Chem. A*, 2015, **119**, 11208–11214.
19 P. Jin, Q. H. Hou, C. C. Tang and Z. F. Chen, *Theor. Chem. Acc.*, 2015, **134**, 1–10.
20 T. R. Yu, Y. Gao, D. X. Xu and Z. G. Wang, *Nano Res.*, 2018, **11**, 354–359.
21 H. Bai, B. Bai, L. Zhang, W. Huang, Y. W. Mu, H. J. Zhai and S. D. Li, *Sci. Rep.*, 2016, **6**, 35518.
22 S. Saha, L. Genovese and S. Goedecker, *Sci. Rep.*, 2017, **7**, 7618.
23 H. R. Li, X. X. Tian, X. M. Luo, M. Yan, Y. W. Mu, H. G. Lu and S. D. Li, *Sci. Rep.*, 2017, **7**, 5701.
24 C. Z. Wang, T. Bo, J. H. Lan, Q. Y. Wu, Z. F. Chai, J. K. Gibson and W. Q. Shi, *Chem. Commun.*, 2018, **54**, 2248–2251.
25 Y. Yang, Z. Zhang, E. S. Penev and B. I. Yakobson, *Nanoscale*, 2017, **9**, 1805–1810.
26 X. Zhou, A. R. Oganov, Z. Wang, I. A. Popov, A. I. Boldyrev and H. Wang, *Phys. Rev. B*, 2016, **93**, 085406.
27 I. V. Getmanskii, R. M. Minyaev, D. V. Steglenko, V. V. Koval, S. A. Zaitsev and V. I. Minkin, *Angew. Chem., Int. Ed.*, 2017, **56**, 10118–10122.
28 *Handbook of Solid State Chemistry*, ed. R. Dronskowski, S. Kikkawa and A. Stein, Wiley-VCH Verlag GmbH & Co. KGaA, 2017, pp. 527–570.
29 J. Wang, W. R. Jiang, W. Y. Xie, J. P. Wang and Z. G. Wang, *Sci. China Mater.*, 2019, **62**, 416–422.
30 X. Zhang, Y. Sun, L. Ma, X. Zhao and X. Yao, *Nanotechnology*, 2018, **29**, 305706.
31 X. Yao, D. Yi and X. Zhang, *J. Mater. Chem. C*, 2019, **7**, 2068–2075.
32 Z. Zhang, E. S. Penev and B. I. Yakobson, *Chem. Soc. Rev.*, 2017, **46**, 6746–6763.
33 Z. Zhang, A. J. Mannix, Z. Hu, B. Kiraly, N. P. Guisinger, M. C. Hersam and B. I. Yakobson, *Nano Lett.*, 2016, **16**, 6622–6627.
34 Z. Zhang, E. S. Penev and B. I. Yakobson, *Nat. Chem.*, 2016, **8**, 525–527.
35 Z. Zhang, Y. Yang, G. Gao and B. I. Yakobson, *Angew. Chem., Int. Ed.*, 2015, **54**, 13022–13026.
36 G. Kresse and J. Furthmuller, *Phys. Rev. B: Condens. Matter Mater. Phys.*, 1996, **54**, 11169–11186.
37 G. Kresse and J. Hafner, *Phys. Rev. B: Condens. Matter Mater. Phys.*, 1993, **47**, 558–561.

38 P. E. Blochl, *Phys. Rev. B: Condens. Matter Mater. Phys.*, 1994, **50**, 17953–17979.
39 G. Kresse and D. Joubert, *Phys. Rev. B: Condens. Matter Mater. Phys.*, 1999, **59**, 1758–1775.
40 J. P. Perdew, K. Burke and M. Ernzerhof, *Phys. Rev. Lett.*, 1996, **77**, 3865–3868.
41 C. Adamo and V. Barone, *J. Chem. Phys.*, 1999, **110**, 6158–6170.
42 M. J. Frisch *et al.*, *Gaussian 09 Revision D.01*, Gaussian Inc., Wallingford CT, 2013.
43 J. VandeVondele, M. Krack, F. Mohamed, M. Parrinello, T. Chassaing and J. Hutter, *Comput. Phys. Commun.*, 2005, **167**, 103–128.
44 T. R. Galeev, B. D. Dunnington, J. R. Schmidt and A. I. Boldyrev, *Phys. Chem. Chem. Phys.*, 2013, **15**, 5022–5029.
45 D. Y. Zubarev and A. I. Boldyrev, *Phys. Chem. Chem. Phys.*, 2008, **10**, 5207–5217.
46 B. D. Dunnington and J. R. Schmidt, *J. Chem. Theory Comput.*, 2012, **8**, 1902–1911.
47 See NBO references and bibliography: www.chem.wisc.edu/nbo5/biblio.htm.
48 K. Momma and F. Izumi, *J. Appl. Crystallogr.*, 2011, **44**, 1272–1276.
49 R. Salcedo, *Polyhedron*, 2009, **28**, 431–436.
50 M. E. Plonska, A. de Bettencourt-Dias, A. L. Balch and K. Winkler, *Chem. Mater.*, 2003, **15**, 4122–4131.
51 R. E. Hughes, C. H. L. Kennard, D. B. Sullenger, H. A. Weakliem, D. E. Sands and J. L. Hoard, *J. Am. Chem. Soc.*, 1963, **85**, 361–362.
52 Y. W. Mu, *J. Phys. Chem. C*, 2015, **119**, 20911–20916.